Journal of Materials Chemistry A

Improving the Performance for Direct Electrolysis of CO2 in Solid Oxide Electrolysis Cells with Sr1.9Fe1.5Mo0.5O6-δ Electrode via Infiltration of Pr6O11 Nanoparticles

Journal:	*Journal of Materials Chemistry A*
Manuscript ID	TA-ART-01-2023-000186.R1
Article Type:	Paper
Date Submitted by the Author:	20-Mar-2023
Complete List of Authors:	Wang, Wanhua; University of South Carolina, Mechanical Engineering Li, Haixia; University of South Carolina, Mechanical Engineering Regalado Vera, Clarita; Idaho National Laboratory Lin, Jie; University of Science and Technology of China, Materials Science and Technology Park, Ka-Young; University of South Carolina, Mechanical Engineering Lee, Taehee; University of South Carolina, Mechanical Engineering Ding, Dong; Idaho National Laboratory, Energy & Environment Science and Technology Chen, Fanglin; University of South Carolina, Mechanical Engineering

ARTICLE

Improving the Performance for Direct Electrolysis of CO_2 in Solid Oxide Electrolysis Cells with $Sr_{1.9}Fe_{1.5}Mo_{0.5}O_{6-\delta}$ Electrode via Infiltration of Pr_6O_{11} Nanoparticles

Received 00th January 20xx,
Accepted 00th January 20xx

DOI: 10.1039/x0xx00000x

Wanhua Wang[a], Haixia Li[a], Clarita Y. Regalado Vera[b,c], Jie Lin[a], Ka-Young Park[a], Taehee Lee[a], Dong Ding[*b] and Fanglin Chen[*a]

Direct CO_2 electrolysis using solid oxide electrolysis cells (CO_2-SOECs) holds the promise to efficiently convert carbon dioxide to carbon monoxide and oxygen. Cathodes with desirable catalytic activity and chemical stability play a critical role in the development of direct CO_2-SOECs. Although $Sr_2Fe_{1.5}Mo_{0.5}O_{6-\delta}$ (SFM) has exhibited promises for direct CO_2-SOECs due to its redox stability, it suffers from insufficient activity for the CO_2 reduction reaction (CO_2RR). Here we report interface engineering of nanosized Pr_6O_{11} on the SFM cathode obtained through infiltration to promote the CO_2RR performance for direct CO_2-SOECs. The effect of Pr_6O_{11} loading on the performance of CO_2RR is systematically investigated. At 800°C, the current density of the Pr_6O_{11} infiltrated SFM cathode with an optimum Pr_6O_{11} loading of 14.8wt.% reaches 1.61 A/cm^2 at 1.5V, more than doubled than that of the SFM cathode (0.76 A/cm^2) at the same operating conditions. X-ray photoelectron spectroscopy (XPS) characterization and in situ diffuse reflectance infrared Fourier transform spectroscopy (DRIFTS) analysis indicate that the adsorption ability of CO_2 on the SFM cathode has been significantly improved by the formation of Pr_6O_{11}. Temperature-programmed desorption (TPD) of CO_2 measurements further manifest that 14.8wt.%Pr_6O_{11}-SFM cathode has better CO desorption capacity. In addition, polarization resistance of the SFM cathode has significantly decreased with the addition of Pr_6O_{11}. Three-electrode measurement was used to analyze the improved electrode kinetics. These results demonstrate that the formation of Pr_6O_{11} in the SFM cathode through infiltration is a promising approach for increasing CO_2RR activity for CO2-SOECs.

Introduction

The innovation in CO_2 emission reduction and energy conversion technologies has attracted increasing attention from governments and industries due to the severe environmental problems caused by fossil fuel consumption[1,2]. Converting carbon dioxide into a variety of chemicals and high-value fuels can effectively mitigate this global energy security and environmental problems. Electrochemical CO_2 reduction reaction (CO_2RR) using solid oxide electrolysis cells (SOECs) can directly convert CO_2 to CO at the cathode while producing O_2 at the anode under the external voltage[3–6]. The generated CO is a valuable energy carrier that can be further applied as fuel to produce electricity or as the building block for the Fischer-Tropsch process to synthesize various hydrocarbons[7–9]. Consequently, CO_2 electrolysis via SOECs has been widely recognized as one of the most promising and efficient approaches for converting CO_2 into useful materials[10–13].

However, the sluggish electrochemical CO_2 reduction reaction in the cathode has been a bottle-necking barrier for the development of SOECs[14,15]. Extensive efforts have been made in exploring suitable cathode catalysts with good electrical conductivity and chemical/microstructural stability, excellent CO_2 adsorption ability, and enhanced electrocatalytic activity for the CO_2 reduction reaction. Early researchers used the anode material of solid oxide fuel cells (SOFCs), such as Ni-based cermet electrodes, as the cathode material for SOECs. However, this brought up different problems due to the differences in gas atmosphere and reaction process between the two modes. Generally, Ni-based cathode catalysts have high conductivity and excellent catalytic activity for CO_2 reduction[16,17]. However, nickel oxidation, aggregation, and carbon deposition are susceptible to occur under high temperatures during CO_2RR without H_2 or CO as the safe (or protecting) gases, resulting in the decrease of conductivity and degradation of catalytic performance[18–20]. In more recent years, attention has been given to the perovskite-related oxides due to their adequate mixed ionic-electronic conductivities, high redox stability, and good coking resistance[21–23]. Among various perovskite oxides studied, $Sr_2Fe_{1.5}Mo_{0.5}O_{6-\delta}$ (SFM) with a double perovskite structure has shown excellent structural stability and adequate electrical conductivity in both oxidizing and reducing atmospheres, making it a promising electrode material for symmetrical solid oxide fuel cells[24,25]. Furthermore, for direct CO_2 electrolysis, $La_{0.9}Sr_{0.1}Ga_{0.8}Mg_{0.2}O_{3-\delta}$ (LSGM) supported single cells with SFM

[a] A Department of Mechanical Engineering, University of South Carolina, Columbia, SC, 29208, USA.
[b] Energy & Environmental Science and Technology, Idaho National Laboratory, Idaho Falls, ID, 83415, USA.
[c] Department of Chemical & Materials Engineering, New Mexico state University, Las Cruses, NM, 88003, USA.
*Corresponding author: Email: dong.ding@inl.gov (D.D.); chenfa@cec.sc.edu (F.C)
Electronic Supplementary Information (ESI) available: [details of any supplementary information available should be included here]. See DOI: 10.1039/x0xx00000x

cathode and $La_{0.9}Sr_{0.1}Co_{0.8}Fe_{0.2}O_{3-\delta}$ (LSCF)-$Sm_{0.2}Ce_{0.8}O_{1.9}$ (SDC) oxygen electrode has achieved a current density of 0.71 A cm^{-2} at 1.5 V and 800°C[26], much higher than those reported using other single perovskite oxides catalysts such as $La_{0.3}Sr_{0.7}Fe_{0.7}Cr_{0.3}O_{3-\delta}$ (0.32 A cm^{-2})[27] and $La_{0.75}Sr_{0.25}Cr_{0.5}Mn_{0.5}O_{3-\delta}$ (0.1 A cm^{-2})[28] for CO_2 conversion under similar testing conditions.

Various strategies have been developed to improve the electrocatalytic activity for direct CO_2 conversion. One of the most popular methods is doping in the A-site, B-site, or O-site of the ABO_3 perovskite structure. By partially replacing Fe with Mn ions, $Sr_2Fe_{1.4}Mn_{0.1}Mo_{0.5}O_{6-\delta}$ (SFMM) presented a similar redox stability to SFM but improved oxygen transport and CO_2 adsorption ability[29]. Besides the doping method, Li and his co-workers reported that SFM-SDC composite electrode can be applied as the potential cathode for direct CO_2 electrolysis since the number of active sites and three phase boundaries (TPBs) has been greatly increased by mechanically mixing SDC with SFM powders. The current density increased to 1.09 A cm^{-2} compared with the SFM electrode at the same operating conditions[26]. Interface engineering of nanoparticles (NPs) with high catalytic activity is also an effective approach to improve the electrochemical performance of the electrode[30–32]. Lv *et al.* found GDC nanoparticles formed in the SFM cathode surface through infiltration showed good stability for over 60 h at 1.2 V and 800°C. An optimal amount of GDC infiltration is beneficial to the expansion of TPBs and active sites for CO_2 adsorption and electroreduction[33].

Recently, it has been reported that Pr_6O_{11} nanoparticles possess excellent oxygen exchange properties and can be utilized to create highly efficient infiltrated oxygen electrodes for SOFC applications[34–37]. However, to the best of our knowledge, there have been no reports on the application of Pr_6O_{11} nanoparticles through infiltration in cathodes for the CO_2 reduction reaction in SOECs. In this work, nanosized Pr_6O_{11} has been incorporated into the SFM backbone by infiltrating $Pr(NO_3)_3$ solution onto the SFM scaffold. The effects of Pr_6O_{11} nanoparticles on the microstructure, electrocatalytic activity for CO_2 splitting reaction, and physicochemical properties of the Pr_6O_{11}-SFM cathode for direct CO_2 electrolysis have been systematically evaluated.

Experimental

Materials preparation and synthesis

$Sr_{1.9}Fe_{1.5}Mo_{0.5}O_{6-\delta}$ (SFM) powders were synthesized using a combustion method with citric acid and glycine as the chelating and combustion agent, respectively. $Sr(NO_3)_2$ (purity 99.0%+), $Fe(NO_3)_3{\cdot}9H_2O$ (purity 99.95%), and $(NH_4)_6Mo_7O_{24}{\cdot}4H_2O$ (purity 99.0%) were used as the precursor chemicals. The precursors were dissolved in deionized water in a stoichiometric amount. Next, citric acid and glycine were added to the solution at a mole ratio of 1:1.5:2 for metal ions: citric acid: glycine. The solution was stirred using a magnetic bar at 200℃ on a hot plate for about 2h until a gel was obtained. The gel was then heated to 500℃ for about 10min until self-combustion occurred. The resulting ashes were collected, subsequently pulverized and calcined at 1100 °C for 5h to form the desired $Sr_{1.9}Fe_{1.5}Mo_{0.5}O_{6-\delta}$ (SFM) powders.

$Pr(NO_3)_3$ infiltration solution was prepared using glycine as the combustion adjuvant, ethanol and deionized water as the solvent. The mass ratio of $Pr(NO_3)_3{\cdot}6H_2O$ (purity 99.9%) to glycine and ethanol was set at 55wt.%:5wt.%:40wt.%. Deionized water was used to obtain a solution with $Pr(NO_3)_3{\cdot}$concentration of 0.1 mol/L.

Characterization

The crystalline phase structure of the obtained materials was investigated by powder X-ray diffraction (XRD, Rigaku MiniFlex II), equipped with Cu Kα radiations. XRD patterns were recorded over a scanning range of 20-80° with a step size of 0.02° at 40 kV and 200 mA. Scanning electron microscopy (SEM, Zeiss Gemini500 FESEM) was applied for microstructure characterizations. Temperature-programmed desorption of CO_2 (CO_2-TPD) (Micromeritics, AutoChem II) was performed to evaluate the CO_2 desorption behaviour and capability. To eliminate the pre-adsorbed substances, the sample was pre-treated at 300°C in He for 1h. After the temperature was cooled down to 50°C, the gas was switched from He to CO_2, and CO_2 was followed for 2h. Next, using He as the carrier gas, TPD signals were recorded in the temperature range from 50°C to 900°C at a heating rate of 10 °C/min. The elemental distribution and surface element states of the samples were determined by X-ray photoelectron spectroscopy (XPS) (PHI VersaProbe III). In situ diffuse reflectance infrared Fourier transform spectroscopy (DRIFT) (Nicolet iS50) was used to characterize the CO_2 adsorption capability of the electrodes. To check the CO_2 adsorption states of the 14.8wt.%Pr_6O_{11}-SFM and SFM cathodes, thermal gravimetric analysis (TGA, NETZSCH STA 449 F3) was performed from room temperature up to 1000°C with a heating rate of 5 °C min^{-1} under air and CO_2 atmosphere, respectively.

Cell fabrication and measurement

$La_{0.8}Sr_{0.2}Ga_{0.8}Mg_{0.2}O_{3-\delta}$ (LSGM) electrolyte-supported single cells were fabricated to evaluate the CO_2 electrolysis performance. The cell configuration is SFM/LSGM/LSCF, with SFM as the cathode, $(La_{0.6}Sr_{0.4})_{0.95}Co_{0.2}Fe_{0.8}O_{3-\delta}$ (LSCF) as the anode. LSGM electrolyte substrates were prepared by uniaxially dry-pressing commercial LSGM powders (Fuel Cell Materials, USA) under 200 MPa, followed by sintering at 1450°C in air for 10h. The thickness of the sintered LSGM electrolyte pellets is about 310 μm. SFM electrode slurry was prepared by mixing SFM powders and Heraeus binder V006 at a weight ratio of 1:1.5. Commercial LSCF powders (Fuel Cell Materials, USA) were used to prepare the LSCF ink through the same method as that of SFM. The SFM slurry and LSCF slurry was separately brush-painted onto either side of the LSGM electrolyte pellet, followed by firing at 1000°C in air for 2h to obtain SFM and LSCF electrode. The thickness of the SFM or LSCF electrode was about 35 μm and the active area was 0.33 cm^2.

Pr_6O_{11} nanoparticles infiltrated SFM single cells were fabricated by infiltrating $Pr(NO_3)_3$ solution onto the prepared SFM cathode side using a microliter syringe, followed by calcining at 600°C for 2h. Pr_6O_{11} infiltrated SFM electrodes with different weight ratios of 6.1wt.%, 11.2wt.%, 14.8wt.%, and 20.4wt.% were prepared, and these modified cathodes were denoted as xPr_6O_{11}-SFM (x=0, 6.1wt.%, 11.2wt.% , 14.8wt.% and 20.4wt.%) cathodes in this work.

The performance of electrocatalytic CO_2 reduction in SOECs was measured using a homemade device. Au paste was used as the current collector on both cathodes and anodes with silver wire as the lead wire. First, the cell was sealed onto an alumina tube using

conductive adhesive (DAD-87, Shanghai Research Institute of Synthetic Resins, China) and then heated to 200°C for 2h to dry the conductive adhesive. Upon cooling down to room temperature, ceramic adhesive (552-1105, Aremco, USA) was applied outside the periphery of the attached cells. Pure CO_2 with a flow rate of 30 mL min^{-1} was supplied into the cathode side while the LSCF anode side was exposed to the ambient air. Electrochemical impedance spectra (EIS) were collected in a frequency range of 1 MHz to 0.01 Hz with an AC amplitude of 10 mV under open circuit voltage (OCV) conditions. The EIS results were analyzed using DRT tools[38]. I-V curves were tested from 1.6 V to 0.1 V by a sequential step change of 50 mV.

The dense LSGM substrate supported symmetrical cells, with the cell configuration of SFM/LSGM/SFM were also fabricated by the pressing and brush-printing process as described above for the single cells. AC impedance of the symmetrical cells was tested under pure CO_2 atmosphere at 650-800°C with a signal amplitude of 10 mV in the frequency range of 1 MHz-0.01 Hz.

The preparation of three-electrode cell was very similar to that of the symmetrical cell, except that a thicker LSGM electrolyte (~1mm) was used, and the edge of the LSGM electrolyte was brushed with Pt paste as the reference electrode. The three-electrode cell was measured at 800°C under a pure CO_2 atmosphere, and the electrochemical impedance spectra data was recorded at OCV, ±20 mV, ±40 mV, and ±60 mV, respectively.

Result and Discussions

Phase structure, morphology, and valance state characterization

X-ray diffraction (XRD) analysis shows that the as-prepared SFM with A-site cation deficiency can be indexed in a cubic perovskite structure. To investigate the phase structure of praseodymium oxide, which was formed in the SFM substrate through infiltration, the powders from calcination of the praseodymium nitrate solution were collected. Figure 1a shows the XRD pattern of the collected powder and it is well matched with the Pr_6O_{11} (PDF#42-1121) characteristic peaks. Figure 1b reveals that the SFM and Pr_6O_{11} have good chemical compatibility and stability. First, 50wt.% praseodymium nitrate infiltrated SFM powder was fired in the air, and no impurity peaks were observed other than SFM and Pr_6O_{11}, indicating excellent chemical compatibility between SFM and Pr_6O_{11} nanoparticles. The mixture powder was then transferred into a CO_2 atmosphere and heated to 800°C for 5h to investigate chemical stability. The main peaks in the XRD pattern were still indexed to SFM and Pr_6O_{11}, indicating that the mixture of SFM and Pr_6O_{11} was stable in the CO_2 atmosphere. In addition, the compatibility between SFM and LSGM was also checked by mixing the two powders in a 1:1 weight ratio and then calcining the mixture at 1000°C in the air for 2h (the condition used to fabricate the SFM cathode for CO_2 electrolysis in this work). The XRD result was shown in Fig.S1 and no impurity peak appeared, indicating that there were no reactions between SFM and LSGM.

The cross-sectional microstructure of the LSGM supported electrolysis cell with a Pr_6O_{11} modified SFM cathode after electrochemical testing was characterized by scanning electron microscopy, as presented in Fig. S2. The thickness of the dense LSGM electrolyte is about 310 μm, and the porous Pr_6O_{11}-SFM cathode

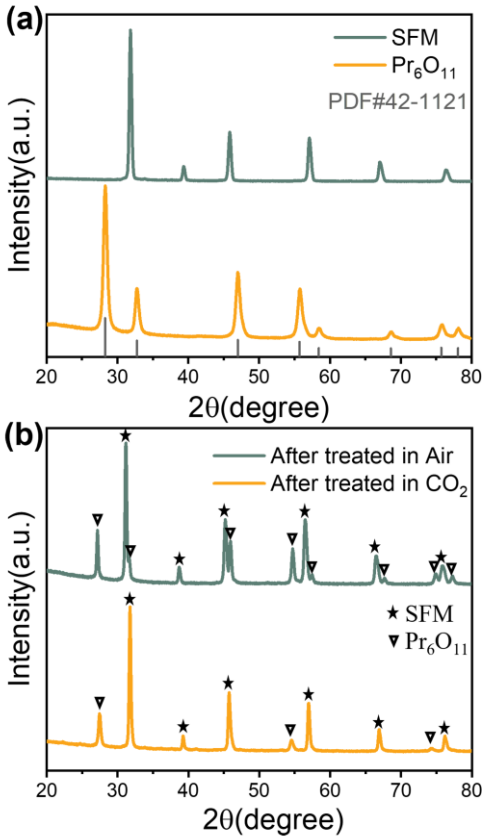

Figure 1. (a) XRD patterns of the as-prepared SFM powder and as-calcined powder from praseodymium nitrate solution, revealing the Pr_6O_{11} phase structure; (b) XRD profiles of the mixture powder of SFM and Pr_6O_{11} treated in air at 1000°C for 2h and then treated in pure CO_2 atmosphere at 800°C for 5h.

layer shows good contact with the LSGM electrolyte layer, as depicted in Fig. S2b. The morphologies of the bare SFM electrode and the Pr_6O_{11} infiltrated SFM electrode are displayed in Fig.2a and Fig. 2b, respectively. The bare SFM cathode shows a uniform, porous and well-connected microstructure. After infiltration, nano-sized Pr_6O_{11} particles can be observed, uniformly distributed on the SFM surface, potentially leading to a significant increase in the number of active sites on the SFM electrode surface.

To further characterize the infiltrated nanoparticles on the SFM electrode, X-ray photoelectron spectra (XPS) were analyzed. As shown in Fig. 2c, Sr, Fe, Mo, and O were detected on the surface of both samples. However, the 14.8wt.% Pr_6O_{11}-SFM sample displayed three additional peaks at the binding energies of 115 eV, 932 eV, and 953 eV respectively, which can be assigned to the Pr signals. As seen in the enlarged XPS survey data (Fig. 2d), Pr3d peaks at around 932 eV and 953 eV can be assigned to $Pr3d_{5/2}$ and $Pr3d_{3/2}$ levels, respectively. The major peaks located at 933.2 eV and 953.2 eV were ascribed to Pr^{4+}. The two shoulder peaks located at 929.2 eV and 948.3 eV can be assigned to Pr^{3+}, which would suggest a considerable concentration of oxygen vacancies. The presence of Pr^{3+} and Pr^{4+} signals demonstrates the coexistence of Pr^{4+} and Pr^{3+}. Based on the XPS results, the ratio of Pr^{4+}/Pr^{3+} was calculated to be about 1.9, which is close to the theoretical ratio of 2 for Pr_6O_{11} and consistent

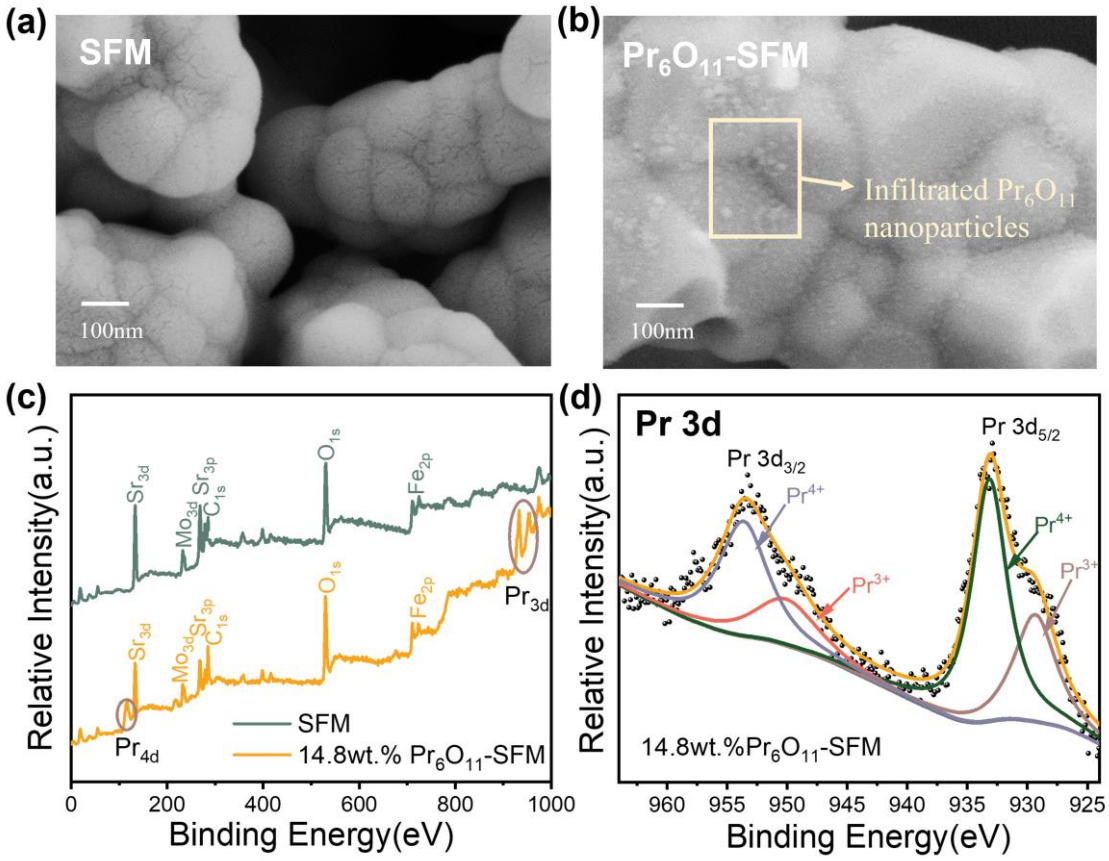

Figure 2. SEM images of (a) SFM electrode, (b) 14.8wt.%Pr_6O_{11}-SFM electrode. XPS profiles of SFM and 14.8wt.%Pr_6O_{11}-SFM samples: (c) the total XPS spectra, and (d) the enlarged Pr3d XPS spectra.

with the XRD results.

CO_2 electrolysis performance

The electrochemical performance of direct CO_2 splitting was compared using SFM electrode infiltrated with different amounts of Pr_6O_{11} by employing single cells with the cell configuration of xPr_6O_{11}-SFM/LSGM/LSCF. Figure 3a presents the relationship between the applied voltage and current density of five types of single cells based on xPr_6O_{11}-SFM (x=0, 6.1wt.%, 11.2wt.%, 14.8wt.% and 20.4wt.%) cathodes at 800°C for direct CO_2 electrolysis. At 800°C, the OCV of the five single cells is around 0.09 V, which is close to those reported in the literature under similar conditions[39–41]. The electrolysis current density increases with the applied voltage, especially when the voltage exceeds 0.9 V, and the current density of the cells with Pr_6O_{11} infiltrated SFM cathodes increases faster than that of the bare SFM, indicating that Pr_6O_{11} can effectively enhance the CO_2 reduction reaction performance compared with the bare SFM electrode. The CO_2RR performance initially improves with increasing the Pr_6O_{11} weight loading to 14.8wt.%, but it begins to decrease when the Pr_6O_{11} loading is further increased to 20.4wt.%. Fig. 3b clearly shows the current density of the five types of SOECs with various Pr_6O_{11} loading amounts under 1.5 V at 800°C. The current density of SOECs with the bare SFM cathode is 0.76 A cm^{-2}, which is close to the results reported in the literature[26]. Under the same testing conditions, the current density of the cell with the 14.8wt.%Pr_6O_{11}-SFM cathode at 1.5 V reaches 1.61 A cm^{-2}, which is more than doubled compared to that of the cells with the bare SFM cathode. Furthermore, under similar measurement conditions, the cell performance of the cells with 14.8wt.%Pr_6O_{11}-SFM cathodes is considerably higher than most of the previously reported results using different cathodes for direct CO_2 electrolysis (Table S1). The CO_2 electrolysis performance of two different types of single cells with 14.8wt.%Pr_6O_{11}-SFM cathode and bare SFM cathode at different temperatures was shown in Fig. S3. Compared with the single cells with the bare SFM cathode, the performance of single cells with 14.8wt.%Pr_6O_{11}-SFM cathode is greatly improved at similar testing conditions.

Electrode kinetics for CO_2RR

To elucidate the origin of enhanced cell performance, the electrochemical impedance spectrum (EIS) was measured from single cells using either bare SFM or 14.8wt.%Pr_6O_{11}-SFM cathode at 800°C under OCV, as shown in Figure 3c. The results were then fitted using an equivalent circuit diagram consisting of R_s (ohmic resistance), CPE (constant phase element), and R_p (total polarization resistance, R_p=R1+R2+R3). The ohmic impedances of the cells with different cathodes are almost identical, indicating that the ohmic resistance predominantly comes from the electrolyte LSGM (which is similar in thickness and microstructure). However, the total polarization resistance of the single cells with the 14.8wt.%Pr_6O_{11}-SFM cathode is 0.81 Ω cm^2, showing a significant reduction compared with that of bare SFM cathode (1.38 Ω cm^2). The polarization resistance of single cells with 14.8wt.%Pr_6O_{11}-SFM cathode at each temperature was also significantly reduced

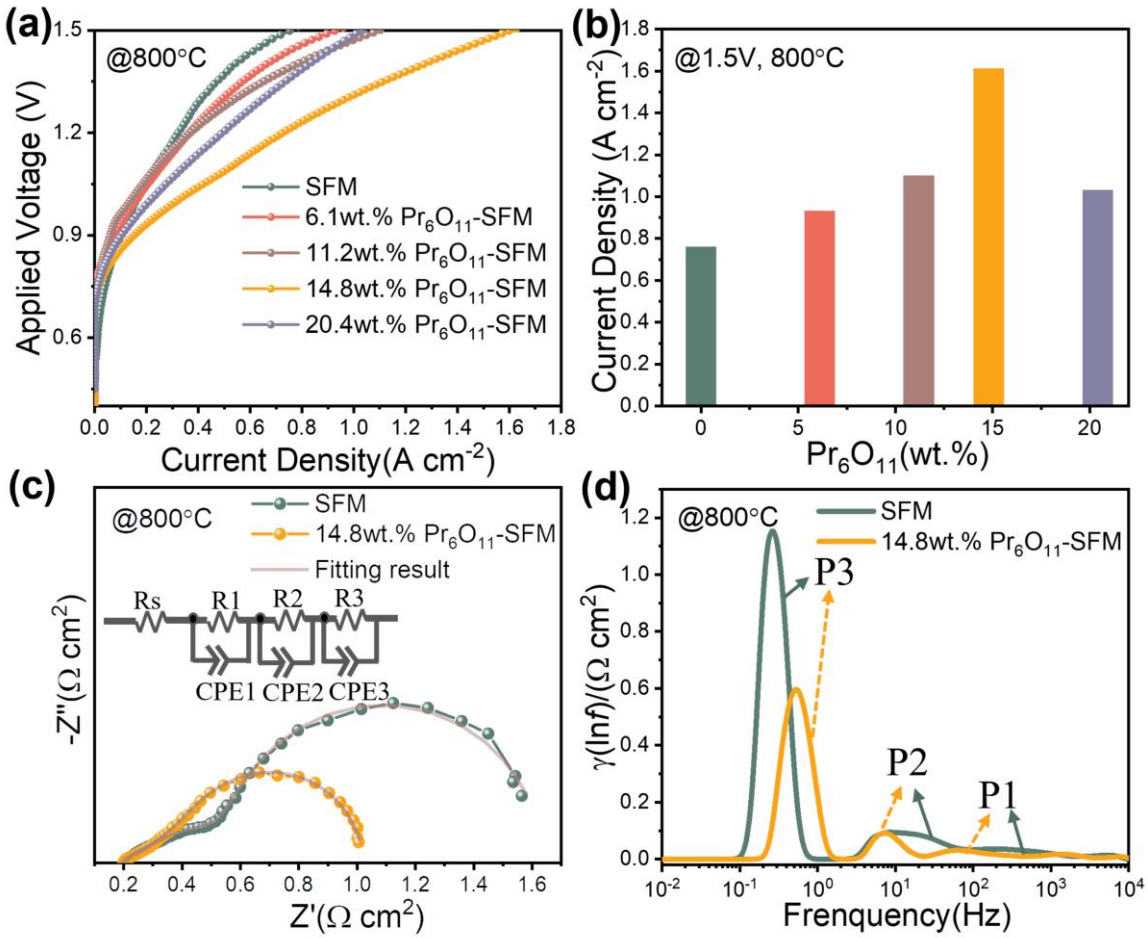

Figure 3. Electrochemical performance comparison of single cells with SFM and Pr_6O_{11}-SFM cathodes. (a) I-V curves of single cells with xPr_6O_{11}-SFM (x=0, 6.1wt.%, 11.2wt.%, 14.8wt.% and 20.4wt.%) cathode at 800°C. (b) Current densities comparison with the different loading of Pr_6O_{11} at 1.5 V and 800°C. (c) Impedance spectra of the SFM and 14.8wt.%Pr_6O_{11}-SFM single cells at 800°C and open circuit voltage condition. (d) Corresponding results from the DRT analysis of the EIS plots in (c).

compared to the bare SFM cathode (Table S2). In order to distinguish the contributions of different CO_2 electrochemical processes, the distribution of relaxation time (DRT) was used to deconvolute the EIS data. DRT is very helpful to isolate the overlapped time constants occurring on the electrodes from the Nyquist plot. The polarization resistance of each sub-step can be calculated by the enclosed area of the corresponding specific peak in the DRT plot. Figure 3d shows the DRT analysis results of the EIS data at 800°C under open circuit voltage conditions. Both DRT curves from the single cells with the different cathodes show three peaks from high to low frequencies, demonstrating that there are at least three sub-steps of the CO_2/CO conversion reactions taking place between the cathode and electrolyte. The three peaks can be marked as high-frequency P1, intermediate-frequency P2, and low-frequency P3. The area of the P1 peaks for the two types of single cells with different cathodes is similar and very small, which could be attributed to the oxygen ion transportation process at the cathode-electrolyte interface[42]. The area of intermediate-frequency P2 and low-frequency P3 for the single cells with 14.8wt.%Pr_6O_{11}-SFM cathode was much smaller than that of the single cells with the bare SFM cathode. P2 may correspond to the sub-step of lattice oxygen diffusivity through the cathode bulk and the oxygen exchange kinetics on the cathode surface[43,44], while P3 should be associated with the gas activation conversion of CO_2/CO, such as surface adsorption and diffusion of active species, as suggested by Adler-Lane-Steele model[45,46]. The much smaller area of P2 and P3 for the single cells with 14.8wt.%Pr_6O_{11}-SFM cathode demonstrates that the infiltrated Pr_6O_{11} nanoparticles on the SFM substrate enhance the carbon dioxide reduction kinetics.

To investigate the interfacial polarization resistance for the CO_2 reduction reaction, EIS was measured in a pure CO_2 atmosphere using symmetrical cells with the cell configurations of 14.8wt.%Pr_6O_{11}-SFM/LSGM/14.8wt.%Pr_6O_{11}-SFM and SFM/LSGM/SFM, respectively. For direct comparison of the polarization resistance, which reflects the catalytic activity towards the CO_2/CO conversion reaction, the ohmic resistance was subtracted, and the first intercept with Z' axis was normalized from zero[47]. As shown in Fig. S4, the R_p values of the symmetrical cells with the bare SFM electrode were 0.95, 1.53, and 2.62 Ω cm^2 at 800, 750, and 700°C, respectively. After infiltration of 14.8wt.%Pr_6O_{11} onto the SFM electrode substrate, the R_p values were reduced to 0.61, 1.09, and 2.18 Ω cm^2 at 800, 750, and 700°C, respectively. There was

approximately a 15-35% reduction in the interfacial polarization resistance at similar testing conditions.

Further, the AC impedance of the three-electrode configuration under various applied voltages at 800°C in a pure CO_2 atmosphere was measured to investigate the electrochemical processes associated with different applied voltages. The schematic diagram of the three-electrode configuration was shown in Fig. S5. The difference between the three-electrode configuration and the symmetrical cell is that the edge of the electrolyte of the three-electrode configuration is coated with Pt slurry as a reference electrode. Figures 4a and 4d show the testing results of three-electrode configuration with either bare SFM electrode cell or 14.8wt.%Pr_6O_{11}-SFM electrode, respectively. It can be seen that under a "positive" overpotential, the polarization resistance values of both cells tend to decrease, indicating faster electrode kinetics at higher applied "positive" voltage[28,48]. However, when a "negative" overpotential was applied, the R_p value obviously increases with the increasing magnitude of the overpotential. To gain insight into this interesting trend, DRT was used to analyze the impedance spectra. Each DRT curve can be broadly divided into three groups of peaks, presenting different electrochemical reaction processes. As shown in Fig. 4(b-c) and 4(e-f), at either positive or negative voltages, the intensity of the high-frequency (HF) peaks of the two cells does not vary much and is irregular, therefore, more attention was paid on the intermedium-frequency (IF) and low-frequency (LF) peaks. With the increase of the applied "positive" voltages, the peak intensities of the LF and IF peaks in both three-electrode cells decrease, demonstrating that the gas reaction and the oxygen exchange kinetics on the working electrode become more rapid with the increase of the driving force from the applied voltage. Moreover, by carefully comparing Fig. 4b and Fig. 4e, the reduction percentage of the 14.8wt.%Pr_6O_{11}-SFM electrode with increasing voltage is larger than that of the SFM electrode, implying that the introduction of Pr_6O_{11} nanoparticles can enhance catalytic activity by expanding the reaction active sites. The LF peak of the 14.8wt.%Pr_6O_{11}-SFM electrode with a much smaller proportion compared to that of the SFM electrode also indicates that the introduction of Pr_6O_{11} nanoparticles will immensely facilitate the gas adsorption and diffusion processes. When switching to "negative" voltage, the two electrodes presented a similar variation trend and both electrodes were dominated by the LF process. The intensity of the LF peaks arises rapidly with the increase of the absolute voltage, while the intensity of the IF peaks changes very slowly. This phenomenon means that the applied "negative" voltage will suppress the gas conversion step.

The reasons why the applied voltage direction will induce different changing tendencies in the electrode polarization resistance may be explained below. Figure 5 shows the schematic diagram of the two modes. When a "positive" voltage is applied between the working electrode (WE) and the reference electrode (RE), electrons will flow from the working electrode to the counter electrode (CE). Sequentially, the CO_2 reduction reaction will take place on the counter electrode, and O^{2-} will be transferred to the working electrode through the LSGM electrolyte. Next, the oxygen evolution reaction (OER) process will proceed on the working electrode. The reactions taking place on the respective electrodes are shown below:

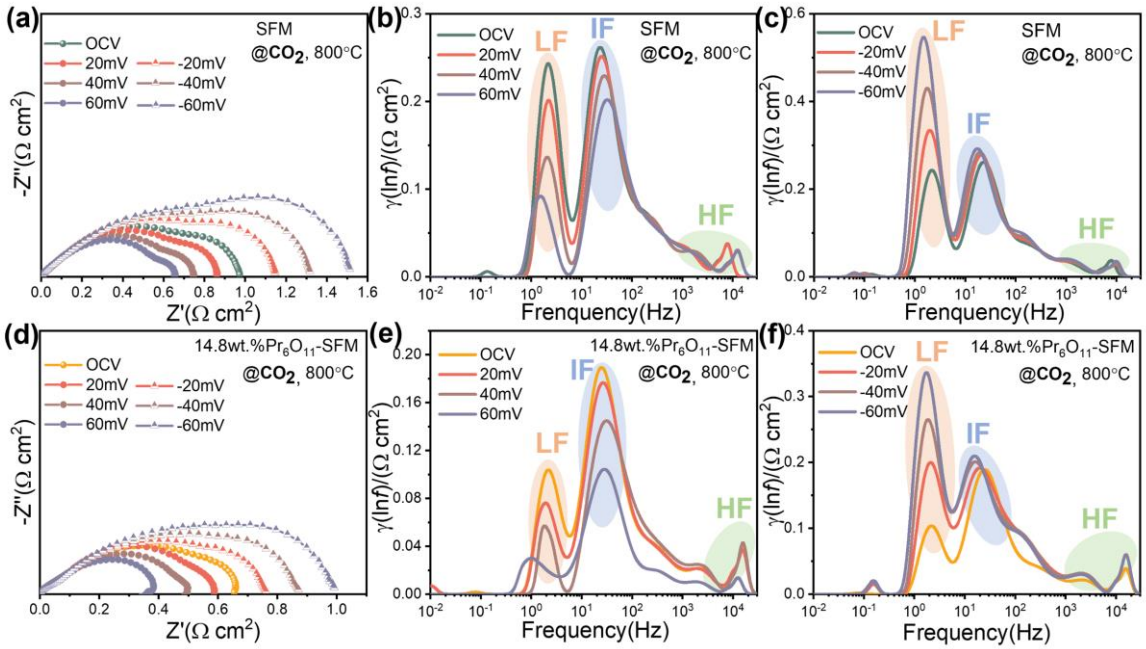

Figure 4. The electrochemical performance comparison of SFM and 14.8wt.%Pr_6O_{11}-SFM cathode material determined with three-electrode cells under pure CO_2 atmosphere in 800°C at different applied voltage. (a) (d) Impedance spectrum of SFM and 14.8wt.%Pr_6O_{11}-SFM three-electrode cells, respectively. (b) (c) DRT analysis of the EIS spectrum for SFM at "positive" and "negative" voltage, respectively. (e) (f) DRT analysis of the EIS spectrum for 14.8wt.%Pr_6O_{11}-SFM at "positive" and "negative" voltage, respectively.

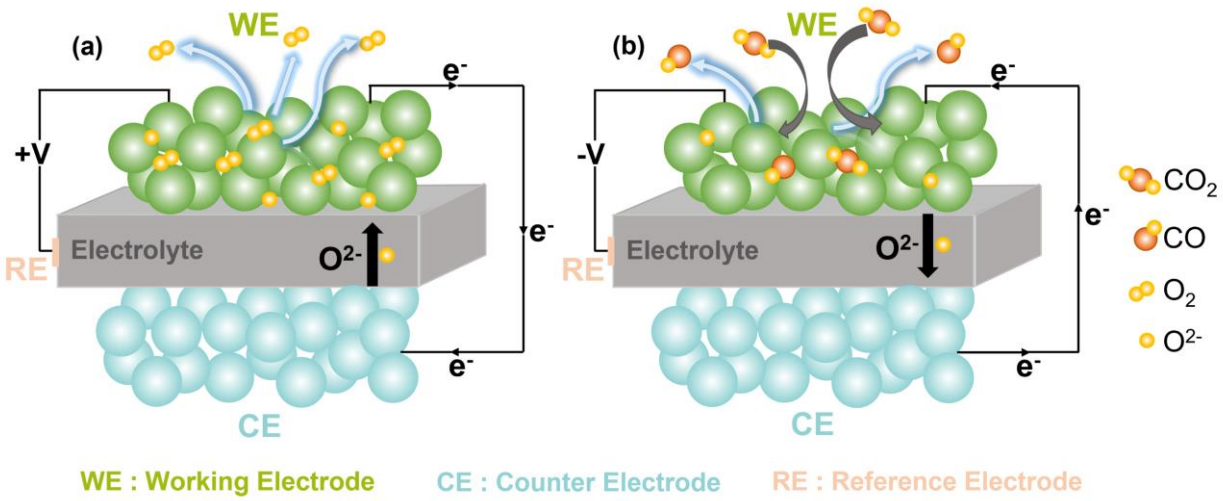

Figure 5. Operation principles of the three electrode cells. (a) The electron flow direction and the reactions occurred on the working electrode when the "positive" voltage is applied. (b) The electron flow direction and the reactions occurred on the working electrode when the "negative" voltage is applied.

Under "Positive" voltage:

WE: $2O^{2-} \longrightarrow 4e^- + O_2$ (1)

CE: $2CO_2 + 4e^- \longrightarrow 2CO + 2O^{2-}$ (2)

However, the direction of the electron flows will be reversed when a "negative" voltage is applied, and the reaction taking place on each electrode will become the opposite:

Under "Negative" voltage:

WE: $2CO_2 + 4e^- \longrightarrow 2CO + 2O^{2-}$ (2)

CE: $2O^{2-} \longrightarrow 4e^- + O_2$ (1)

According to the above-mentioned analysis, the gas reaction on the WE is OER when applying a positive voltage. Increasing the applied voltage will result in faster electron transfer, which promotes the OER rate and O_2 desorption process. This can explain why the intensities of LF and IF peaks decrease when increasing the voltage. However, when applying a negative voltage, CO_2 reduction reaction takes place on the WE, and the CO desorption process will become more difficult because of the larger molecular volume of CO compared to O_2. Furthermore, concentration polarization will form if the CO_2 molecule cannot diffuse rapidly into the reaction zone and CO is not immediately desorbed. The increased intensity of LF peaks can be explained by the more severe concentration polarization when increasing the absolute applied voltage under a negative voltage.

Enhancement of CO_2 adsorption and CO desorption

One of the key steps to initiate CO_2 conversion reaction is the gas/solid interaction including CO_2 adsorption and CO desorption on the electrode surface under direct CO_2 electrolysis. Therefore, the CO_2 adsorption characteristics on SFM and 50wt.%Pr_6O_{11}-SFM powders were measured by thermal gravimetric analysis (TGA) under a CO_2 atmosphere from room temperature to 1000°C. The 50wt.% Pr_6O_{11} loading was chosen to intensify the effect of Pr_6O_{11} on CO_2 adsorption. For comparison, TGA measurement was also conducted in the air atmosphere to eliminate the influence of air. As shown in Fig. 6a, the SFM sample exhibited very slight differences in weight loss in air and CO_2 atmosphere, implying that SFM does not adsorb much CO_2. In contrast, the weight loss of the 50wt.%Pr_6O_{11}-SFM samples in CO_2 is about 3.04wt.% at 800°C, which is 3.97wt.% lower than that in an air atmosphere (7.01wt.%), implying that significant amount of CO_2 was adsorbed during the test. It has been reported that praseodymium oxide possesses high oxygen vacancy concentration[36], which can serve as host sites to accommodate linear CO_2 molecules[49].

To further investigate the surface adsorption properties of CO_2 on the 14.8wt.%Pr_6O_{11}-SFM and bare SFM samples, in situ diffuse reflectance infrared Fourier transform spectroscopy (DRIFT) was carried out at elevated temperatures. As shown in Fig. 6b, there are significant absorption peaks in the range of 1300-1500 cm^{-1} for both samples, which can be typically assigned to CO_3^{2-} on the specimen surface[50–52]. The signals are still visible when the temperature increases to 400°C, demonstrating that the carbonate species are still adsorbed on the sample's surface, and therefore, the adsorbed CO_2 is stable at a high temperature of 400°C. By comparison, the intensity of adsorption peaks of SFM at 100°C is higher than that of 14.8wt.%Pr_6O_{11}-SFM, but it becomes weaker than that of 14.8wt.%Pr_6O_{11}-SFM at elevated temperatures, illustrating that the introduction of Pr_6O_{11} nanoparticles can increase the CO_2 adsorption capability at higher temperatures. The CO_2-TPD results also support this viewpoint. Figure 6c presents the TPD curves in the CO_2 atmosphere from room temperature to 900°C. There are two desorption peaks for the SFM sample: the one below 200°C corresponds to the release of physisorbed CO_2, while the other one located around 397°C could be ascribed to the monodentate, bidentate, and tridentate as well as carbonates[53], which are the decomposition products of chemisorbed CO_2. Apparently, for the 14.8wt.%Pr_6O_{11}-SFM sample, not only is the intensity of the desorption peak much stronger than that of the bare SFM sample, but there is also one more desorption peak at 781°C, suggesting enhanced bonding of the adsorbed CO_2. This result indicates that the

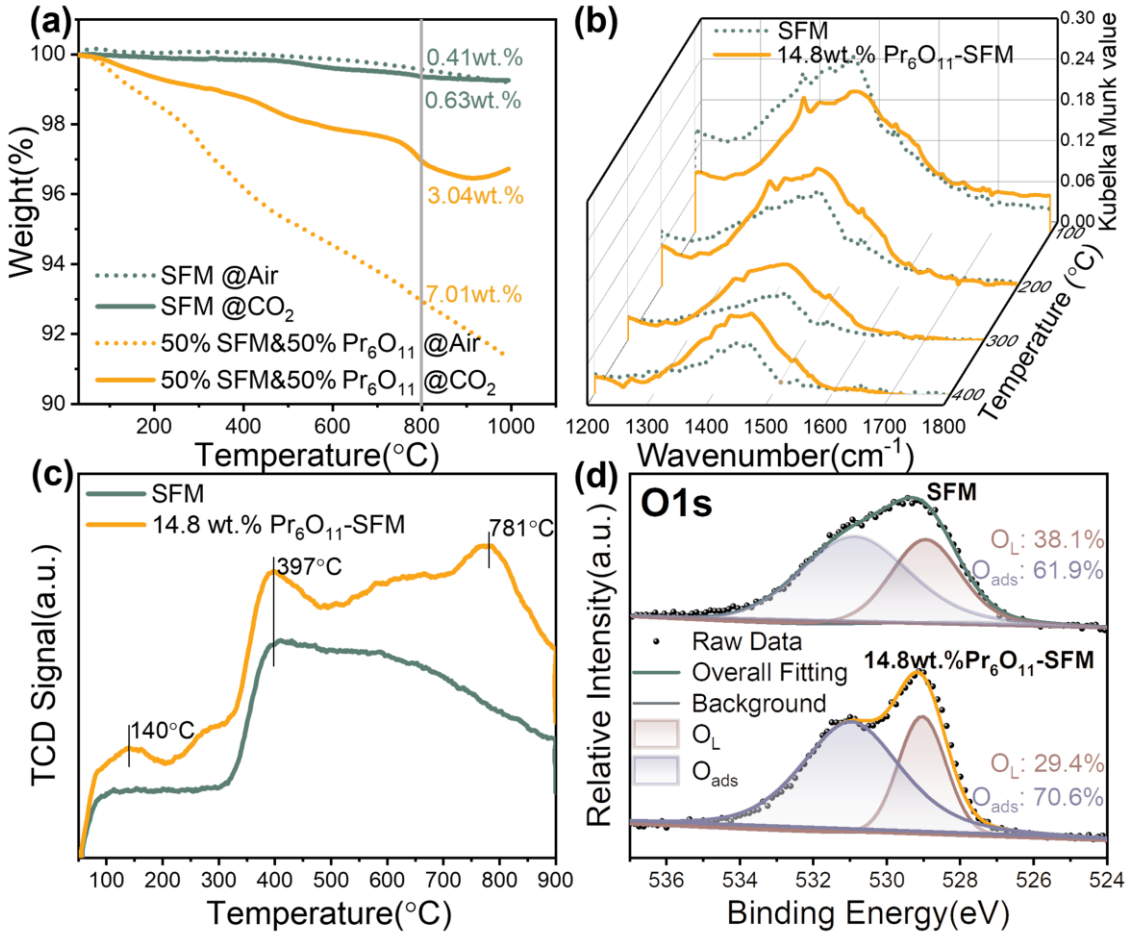

Figure 6. Physicochemical characterization of as-prepared SFM and Pr_6O_{11}-SFM samples. (a) Thermal gravimetric analysis curves of SFM and 50wt.%Pr_6O_{11}-50wt.%SFM samples. (b) In situ diffuse reflectance infrared Fourier transform spectroscopy for the surface adsorption properties of CO_2 linear molecules on the SFM and 14.8wt.%Pr_6O_{11}-SFM samples. (c) Temperature programmed desorption profiles for CO_2 on the surface of SFM and 14.8wt.%Pr_6O_{11}-SFM powder. (d) High-resolution O1s XPS spectra for the SFM and 14.8wt.%Pr_6O_{11}-SFM powder.

infiltration of Pr_6O_{11} nanoparticles adds new adsorption active sites on the SFM substrate, thus promoting the CO_2 adsorption ability and further improving the CO_2 electrochemical reaction.

The kinetics of the CO_2 splitting reaction are closely related to the electronic structure of the electrocatalyst. XPS characterizations were thus performed on O-1s spectra. As shown in Figure 6d, the high-resolution O1s spectra of the 14.8wt.%Pr_6O_{11}-SFM sample and the bare SFM sample reveal two main fitting peaks, meaning the presence of two types of oxygen species. The peak at around 529.1 eV can be assigned to the lattice oxygen species (O_L) while the peak at approximately 531.2 eV corresponds to the adsorbed oxygen species (O_{ads}) such as O^{2-} and carbonates, et al[54,55]. After infiltrating Pr_6O_{11} to the SFM substrate, the content of adsorbed oxygen species on the sample's surface apparently increased from 61.9% to 70.6%, implying that the infiltrated Pr_6O_{11} nanoparticles generated more than 8% of additional surface-adsorbed oxygen-containing species compared to the bare SFM sample. The increased O_{ads} content in 14.8wt.%Pr_6O_{11}-SFM is of great importance in the CO_2 electrochemical reaction since these adsorbed oxygen species can be easily liberated under elevated temperatures. This structural feature can lead to the generation of abundant active sites on the outer surface of the material, which is conducive to the surface adsorption of CO_2 at elevated temperatures[56,57]. In addition, chemisorbed CO_2 can be activated in oxygen vacancies, contributing to the improved kinetics of carbon dioxide electrolysis[58].

Long-term stability

The durability of single cells with either SFM or 14.8wt.%Pr_6O_{11}-SFM cathode for CO_2RR was evaluated by monitoring the cell voltage under a constant current load of 910 mA/cm^2 at 800°C. The effect of the infiltrated praseodymium oxide to SFM on long-term stability was investigated, and the results are presented in Fig. 7. There is no obvious performance degradation after 100 hours of testing, indicating excellent electrochemical stability of both types of single cells during the testing period. The cross-sectional image of single cells with 14.8wt.%Pr_6O_{11}-SFM cathode after 100h CO_2 electrolysis measurement (Fig. S2c) shows that the 14.8wt.%Pr_6O_{11}-SFM electrode maintains a good bonding with the LSGM electrolyte.

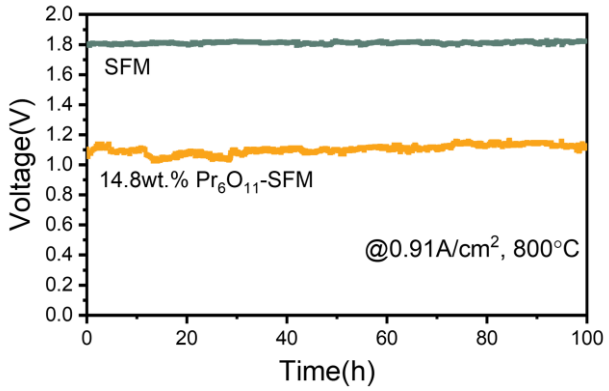

Figure 7. The durability test under constant current densities at 800°C for SFM and 14.8wt.%Pr_6O_{11}-SFM single cells.

Furthermore, the voltage of the single cells with the 14.8wt.%Pr_6O_{11}-SFM cathode at 910 mA/cm^2 is much lower than that of bare SFM cathode under the same testing conditions, indicating that the single cell using14.8wt.%Pr_6O_{11}-SFM cathode exhibits much better performance than those of SFM, which is consistent with the results of the IV curves.

Conclusion

In summary, SFM with and without Pr_6O_{11} nanoparticles has been evaluated as cathodes for direct CO_2 electrolysis in SOECs. The introduction of Pr_6O_{11} to SFM enhances CO_2 reduction reaction performance and the 14.8wt.% loading of Pr_6O_{11} is an optimum amount. When 14.8wt.% Pr_6O_{11}-SFM was applied as the cathode in LSGM electrolyte-supported SOECs for direct CO_2 electrolysis, a current density of 1.61 A cm^{-2} was achieved at 1.5 V and 800°C, which was 2.1 times that of SOECs with the bare SFM cathode under similar testing conditions. The enhanced electrocatalytic activity of the 14.8wt.% Pr_6O_{11}-SFM cathode can be attributed to the enlarged TPB lengths after the infiltration of Pr_6O_{11} nanoparticles, resulting in additional active sites for CO_2 adsorption and enhancement for CO desorption. The present study demonstrates that praseodymium oxide infiltration to perovskite substrate is a promising approach to enhance the cathode performance for direct electrolysis of CO_2 in SOECs.

Author Contributions

F.C. and W.W. conceived the idea, designed the experiments, and analyzed the data. W.W. drafted the manuscript. F.C. and D.D. reviewed the manuscript and contributed to the final version of the manuscript. H.L. and C.V. performed the materials preparation and characterization. J.L., K.P., and T.L. participated in the data analysis.

Conflicts of interest

There are no conflicts to declare.

Acknowledgements

Financial support from the U.S. Department of Energy (DE-EE0009427) and NASA EPSCoR (Grant # 80NSSC20M0233) is greatly appreciated. D.D. would like to thank the funding support by the U.S. Department of Energy (USDOE), Office of Energy Efficiency and Renewable Energy (EERE), Advanced Manufacturing Office (AMO) under DOE Idaho Operations Office under Contract No. DE-AC07-05ID14517.

Notes and References

1 Z. Yang, Z. Lei, B. Ge, X. Xiong, Y. Jin, K. Jiao, F. Chen and S. Peng, *Int. J. Coal Sci. Technol.*, 2021, **8**, 377–382.
2 D. Huan, L. Zhang, S. Zhang, N. Shi, X. Li, K. Zhu, C. Xia, R. Peng and Y. Lu, *J. Mater. Chem. A*, 2021, **9**, 2706–2713.
3 A. Hauch, R. Küngas, P. Blennow, A. B. Hansen, J. B. Hansen, B. V. Mathiesen and M. B. Mogensen, *Science (80-.).*, 2020, **370**, eaba6118.
4 Y. Song, X. Zhang, K. Xie, G. Wang and X. Bao, *Adv. Mater.*, 2019, **31**, 1902033.
5 Y. Li, W. Zhang, Y. Zheng, J. Chen, B. Yu, Y. Chen and M. Liu, *Chem. Soc. Rev.*, 2017, **46**, 6345–6378.
6 W. Bian, W. Wu, B. Wang, W. Tang, M. Zhou, C. Jin, H. Ding, W. Fan, Y. Dong and J. Li, *Nature*, 2022, **604**, 479–485.
7 Y. Wang, T. Liu, S. Fang, G. Xiao, H. Wang and F. Chen, *J. Power Sources*, 2015, **277**, 261–267.
8 Q. Fu, C. Mabilat, M. Zahid, A. Brisse and L. Gautier, *Energy Environ. Sci.*, 2010, **3**, 1382–1397.
9 C. M. Stoots, J. E. O'Brien, J. S. Herring and J. J. Hartvigsen, .
10 Y. Li, P. Li, B. Hu and C. Xia, *J. Mater. Chem. A*, 2016, **4**, 9236–9243.
11 C. Graves, S. D. Ebbesen, M. Mogensen and K. S. Lackner, *Renew. Sustain. Energy Rev.*, 2011, **15**, 1–23.
12 M. Li, B. Hua, L.-C. Wang, J. D. Sugar, W. Wu, Y. Ding, J. Li and D. Ding, *Nat. Catal.*, 2021, **4**, 274–283.
13 X. Xi, Y. Fan, J. Zhang, J.-L. Luo and X.-Z. Fu, *J. Mater. Chem. A*, 2022, **10**, 2509–2518.
14 C. Sun, L. Bian, J. Qi, W. Yu, S. Li, Y. Hou, L. Wang, J. Peng and S. An, *J. Power Sources*, 2022, **521**, 230984.
15 A. Nechache and S. Hody, *Renew. Sustain. Energy Rev.*, 2021, **149**, 111322.
16 G. Tsekouras and J. T. S. Irvine, *J. Mater. Chem.*, 2011, **21**, 9367–9376.
17 Z. Li, M. Peng, Y. Zhu, Z. Hu, C.-W. Pao, Y.-C. Chang, Y. Zhang, Y. Zhao, J. Li and Y. Sun, *J. Mater. Chem. A*, 2022, **10**, 20350–20364.
18 Y. Jiang, F. Chen and C. Xia, *J. Power Sources*, 2021, **493**, 229713.
19 S.-D. Kim, D.-W. Seo, A. K. Dorai and S.-K. Woo, *Int. J. Hydrogen Energy*, 2013, **38**, 6569–6576.
20 S. D. Ebbesen and M. Mogensen, *J. Power Sources*, 2009, **193**, 349–358.
21 X. Zhang, Y. Song, G. Wang and X. Bao, *J. Energy Chem.*, 2017, **26**, 839–853.
22 Z. Cao, B. Wei, J. Miao, Z. Wang, Z. Lü, W. Li, Y. Zhang, X. Huang, X. Zhu, Q. Feng and Y. Sui, *Electrochem. commun.*, 2016, **69**, 80–83.
23 H. M. Ansari, A. S. Bass, N. Ahmad and V. I. Birss, *J. Mater. Chem. A*, 2022, **10**, 2280–2294.
24 A. B. Muñoz-García, D. E. Bugaris, M. Pavone, J. P. Hodges, A. Huq, F. Chen, H.-C. zur Loye and E. A. Carter, *J. Am. Chem. Soc.*, 2012, **134**, 6826–6833.
25 Q. Liu, D. E. Bugaris, G. Xiao, M. Chmara, S. Ma, H.-C. zur Loye, M. D. Amiridis and F. Chen, *J. Power Sources*, 2011, **196**, 9148–9153.
26 Y. Li, X. Chen, Y. Yang, Y. Jiang and C. Xia, *ACS Sustain. Chem. Eng.*, 2017, **5**, 11403–11412.

27 P. K. Addo, B. Molero-Sanchez, M. Chen, S. Paulson and V. Birss, *Fuel cells*, 2015, **15**, 689–696.
28 S. Xu, S. Li, W. Yao, D. Dong and K. Xie, *J. Power Sources*, 2013, **230**, 115–121.
29 Y. Jiang, Y. Yang, C. Xia and H. J. M. Bouwmeester, *J. Mater. Chem. A*, 2019, **7**, 22939–22949.
30 Y. Chen, Y. Choi, S. Yoo, Y. Ding, R. Yan, K. Pei, C. Qu, L. Zhang, I. Chang and B. Zhao, *Joule*, 2018, **2**, 938–949.
31 Y. Nishihata, J. Mizuki, T. Akao, H. Tanaka, M. Uenishi, M. Kimura, T. Okamoto and N. Hamada, *Nature*, 2002, **418**, 164–167.
32 D. Ding, X. Li, S. Y. Lai, K. Gerdes and M. Liu, *Energy Environ. Sci.*, 2014, **7**, 552–575.
33 H. Lv, Y. Zhou, X. Zhang, Y. Song, Q. Liu, G. Wang and X. Bao, *J. Energy Chem.*, 2019, **35**, 71–78.
34 C. Nicollet, A. Flura, V. Vibhu, A. Rougier, J.-M. Bassat and J.-C. Grenier, *Int. J. Hydrogen Energy*, 2016, **41**, 15538–15544.
35 M. Khoshkalam, M. A. Faghihi-Sani, X. Tong, M. Chen and P. V. Hendriksen, *J. Electrochem. Soc.*, 2020, **167**, 24505.
36 H. Chen, Z. Guo, L. A. Zhang, Y. Li, F. Li, Y. Zhang, Y. Chen, X. Wang, B. Yu and J. Shi, *ACS Appl. Mater. Interfaces*, 2018, **10**, 39785–39793.
37 Y. Chen, Y. Chen, D. Ding, Y. Ding, Y. Choi, L. Zhang, S. Yoo, D. Chen, B. Deglee and H. Xu, *Energy Environ. Sci.*, 2017, **10**, 964–971.
38 T. H. Wan, M. Saccoccio, C. Chen and F. Ciucci, *Electrochim. Acta*, 2015, **184**, 483–499.
39 Y. Xie, J. Xiao, D. Liu, J. Liu and C. Yang, *J. Electrochem. Soc.*, 2015, **162**, F397.
40 C. Ruan and K. Xie, *Cite this Catal. Sci. Technol*, 2014, **5**, 1929.
41 G. Tao, K. R. Sridhar and C. L. Chan, *Solid State Ionics*, 2004, **175**, 621–624.
42 Y. Li, B. Hu, C. Xia, W. Q. Xu, J. P. Lemmon and F. Chen, *J. Mater. Chem. A*, 2017, **5**, 20833–20842.
43 Y. Li, Y. Li, S. Zhang, C. Ren, Y. Jing, F. Cheng, Q. Wu, P. Lund and L. Fan, *Cite This ACS Appl. Mater. Interfaces*, 2022, **14**, 9150.
44 L. Duranti, I. Luisetto, S. Licoccia, C. D'Ottavi and E. Di Bartolomeo, *J. Electrochem. Soc.*, 2021, **168**, 104507.
45 S. B. Adler, *Chem. Rev.*, 2004, **104**, 4791–4844.
46 S. B. Adler, J. A. Lane and B. C. H. Steele, *J. Electrochem. Soc.*, 1996, **143**, 3554.
47 X. Meng, Y. Wang, Y. Zhao, T. Zhang, N. Yu, X. Chen, M. Miao and T. Liu, *Electrochim. Acta*, 2020, **348**, 136351.
48 X. Yue and J. T. S. Irvine, *Electrochem. solid-state Lett.*, 2012, **15**, B31.
49 J. Zhu, W. Zhang, Y. Li, W. Yue, G. Geng and B. Yu, *Appl. Catal. B Environ.*, 2020, **268**, 118389.
50 L. Ye, M. Zhang, P. Huang, G. Guo, M. Hong, C. Li, J. T. S. Irvine and K. Xie, *Nat. Commun.*, 2017, **8**, 1–10.
51 J. Lu, C. Zhu, C. Pan, W. Lin, J. P. Lemmon, F. Chen, C. Li and K. Xie, *Sci. Adv.*, 2018, **4**, eaar5100.
52 H. Du, C. T. Williams, A. D. Ebner and J. A. Ritter, *Chem. Mater.*, 2010, **22**, 3519–3526.
53 D. Schweke, S. Zalkind, S. Attia and J. Bloch, *J. Phys. Chem. C*, 2018, **122**, 9947–9957.
54 W. Wang, Y. Yang, D. Huan, L. Wang, N. Shi, Y. Xie, C. Xia, R. Peng and Y. Lu, *J. Mater. Chem. A*, 2019, **7**, 12538–12546.
55 X. Xi, X.-W. Wang, Y. Fan, Q. Wang, Y. Lu, J. Li, L. Shao, J.-L. Luo and X.-Z. Fu, *J. Power Sources*, 2021, **482**, 228981.
56 X. Xi, J. Liu, Y. Fan, L. Wang, J. Li, M. Li, J.-L. Luo and X.-Z. Fu, *Nano Energy*, 2021, **82**, 105707.
57 Y. Li, Y. Li, Y. Wan, Y. Xie, J. Zhu, H. Pan, X. Zheng and C. Xia, *Adv. Energy Mater.*, 2019, **9**, 1803156.
58 X. Yang, K. Sun, M. Ma, C. Xu, R. Ren, J. Qiao, Z. Wang, S. Zhen, R. Hou and W. Sun, *Appl. Catal. B Environ.*, 2020, **272**, 118968.